Short communication

Modelling of solid oxide steam electrolyser: Impact of the operating conditions on hydrogen production

J. Laurencin[a,*], D. Kane[a], G. Delette[a], J. Deseure[b], F. Lefebvre-Joud[a]

[a] CEA/LITEN, 17 rue des martyrs, 38054 Grenoble, France
[b] LEPMI, UMR 5631 CNRS-INPG-UJF, 1130 rue de la piscine, BP 75, 38402 Saint Martin d'Hères, France

ABSTRACT

A 2D multi-physic in-house-model has been developed to analyse the performances of Solid Oxide Electrolysis Cell (SOEC) stack. This model encompasses a combined electrochemical and thermal description of the electrolyser. An analytical solution for multi-species diffusion across the porous cathode has been implemented in the model. This numerical tool is useful to provide all the important parameters of the stack operation: distribution of temperature, heat fluxes, local current densities, gas concentrations and overpotentials.

Simulations show that thermal equilibrium of the stack is strongly dependant on radiative heat losses, whereas convective heat transfers are limited. In the exothermic operation mode, the cell warming depends on the radiation efficiency.

A parametric study has been carried out to analyse SOEC irreversible losses. It is found that the anode activation overpotential is significant, whereas the polarisation due to the cathode activation remains much more limited. Anode concentration overpotentials are found to be insignificant whatever the operating condition. Cathode concentration overpotentials are found to be moderate in the case of Electrolyte Supported Cell (ESC), while they can increase drastically with current density in the case of Cathode Supported Cell (CSC). Addition of diluent gases into the H_2, H_2O mixture is found to increase the concentration overpotentials.

© 2010 Elsevier B.V. All rights reserved.

1. Introduction

In the context of fossil fuel rarefaction, hydrogen is considered as a promising energy carrier liable to complement or even replace fossil hydrocarbon fuel [1]. When driven by renewable or nuclear energy, water electrolysis allows producing "clean" hydrogen without greenhouse gas emission. The energy required for low temperature water electrolysis, either with acidic or alkaline electrolyte, has to be entirely provided as electricity. For high temperature water electrolysis, namely High Temperature Steam Electrolysis (HTSE), the energy required is lower because the water molecules are already gaseous. Moreover part of this energy can be brought as heat [2]. As a result, when heat sources are available HTSE stands as a highly relevant hydrogen production mode [3–5]. Furthermore, the high temperature allows avoiding the use of expensive catalysts for the electrochemical reactions.

The steam electrolysis reaction (1) is the reverse operation of Solid Oxide Fuel Cells (SOFC). At the cathode side, water is reduced according to the electrochemical reaction (1a) written in the case of an anion conducting electrolyte, whereas oxygen is produced at the anode side through reaction (1b):

$$H_2O \rightarrow 1/2O_2 + H_2 \qquad \Delta H^0(800\,°C) = +242\,KJ\,mol^{-1} \qquad (1)$$

$$H_2O + 2e^- \rightarrow H_2 + O^{2-} \qquad (1a)$$

$$O^{2-} \rightarrow 1/2O_2 + 2e^- \qquad (1b)$$

The feasibility of the electrolysis operation has been demonstrated in the 80s by Dornier using tubular cells [6]. More recently, planar SOFC cells, SRUs and short stacks operated in the electrolyser mode have given promising hydrogen production rates [7,8]. In these studies, Solid Oxide Electrolysis Cells (SOEC) are constituted by the same ceramic assembly as SOFC: the dense electrolyte is classically made of Yttria Stabilised Zirconia (YSZ), porous Lanthanum doped Strontium Manganite (LSM) is used for the anode and a porous cermet composed of YSZ and Nickel (Ni-YSZ) is used for the cathode. In planar configuration, cells are stacked into a high packing density and are separated by stainless steel plates, ensuring the electrical inter-connection and gas distribution on the electrodes. However, if high performance levels have been obtained by operating SOFC in the electrolyser mode, some limitations have also been highlighted regarding SOEC durability either at the single cell level [8] or when integrated into a stack [9,10].

* Corresponding author. Tel.: +33 4 38782210; fax: +33 4 38784139.
E-mail address: laurencin@chartreuse.cea.fr (J. Laurencin).

List of symbols

a	manifold width (cm)
b	manifold height (cm)
L	manifold length (cm)
C_p^i	heat capacity (J mol^{-1} K^{-1})
$D_{i,j}^{eff}$	effective molecular diffusion coefficient (cm^2 s^{-1})
$D_{i,k}^{eff}$	effective Knudsen diffusion coefficient (cm^2 s^{-1})
D_i^{eff}	effective diffusion coefficient (cm^2 s^{-1})
$E_{i=0}$	Open Circuit Voltage (mV)
F	Faraday constant (=96485 C mol^{-1})
h	heat transfer coefficient (W m^{-2} K^{-1})
i	local current density (mA cm^{-2})
i_0	exchange current density (mA cm^{-2})
n_i	molar flow rate (mol s^{-1})
N_i	molar flux (mol s^{-1} cm^{-2})
$\bar{r}$	mean pore radius (μm)
R	gas constant (=8.314 J mol^{-1} K^{-1}) or H$_2$/H$_2$O ratio
R_{ohm}	ohmic resistance (Ω cm^2)
R_C	contact resistance (Ω cm^2)
R_{LSM}	electrical resistance of anode (Ω cm^2)
$R_{Ni\text{-}8YSZ}$	electrical resistance of cathode (Ω cm^2)
T	temperature (K)
U	cell voltage (mV)
y_i	molar fraction
δ_a	anode thickness (cm)
δ_c	cathode thickness (cm)
δ_e	electrolyte thickness (cm)
ΔH_r	reaction enthalpy (J mol^{-1})
λ	thermal conductivity (W m^{-1} K^{-1})
η	dynamic viscosity (kg m^{-1} s^{-1})
η_{act}	anode or cathode activation overpotentials (mV)
η_{conc}	anode or cathode concentration overpotentials (mV)
ε	porosity or emissivity
τ	tortuosity factor
ρ	electrical conductivity (Ω^{-1} cm^{-1})
σ	Stefan–Boltzmann's constant (=5.67 × 10^{-8} W m^{-2} K^{-4})
ξ	cathodic gas dilution rate

Computing simulation appears to be one of the most efficient approaches to analyse the coupled mechanisms of SOEC operation. Indeed, the cell response depends on multi-physic phenomena which are entangled such as the electrochemical reactions, mass and energy transport in the electrolyser. Some models have been recently developed to describe the SOEC behaviour. Ni et al. [11,12] have proposed isothermal models taking into account the coupled mass transport and electrochemical reactions. In reference [12], diffusion of H$_2$O and H$_2$ species at the cathode side are described through the Dusty Gas Model (DGM). Udagawa et al. [13,14] have developed a one dimensional dynamic model including a thermal analysis. For design optimisation, commercial Computational Fluid Dynamic (CFD) software has been used by Herring et al. [15] to propose a three dimensional SOEC modelling. Freshly, Gondrin et al. [16] have improved the two dimensional CFD description by implementing the DGM approach to calculate H$_2$ and H$_2$O distribution through porous cathode as a function of microstructure.

In the present work, an in-house model has been developed to describe the thermo-electrochemical behaviour of a planar SOEC stack. A two dimensional approach has been adopted in order to couple locally fluidic, thermal and electrochemical steps. This SOEC model is derived from a first one previously developed for SOFC operation simulation [17,18]. The mass transfer into the porous electrodes has been described in the frame of the DGM model. At the cathode side, the effect of gas dilution has been taken into account by adding nitrogen into the H$_2$O/H$_2$ mixture. Mass transport and kinetics of electrochemical reactions have been coupled to a ther-
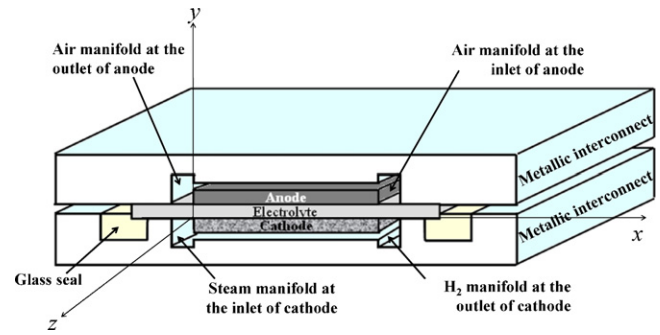

Fig. 1. Schematic representation of the simulated SRU (cross-section view) and coordinate system used in the model.

mal analysis. A special attention has been paid on radiative heat losses that are usually neglected despite their significant influence. Mechanisms of steam electrolysis and cell operation have been analysed. The effects of H$_2$/H$_2$O ratio introduced at the cathode inlet and the impact of gas dilution on the electrolyser efficiency have been investigated.

2. Model description

2.1. Introduction: geometry and materials

A schematic cross-section of the simulated Single Repeat Unit (SRU) is illustrated in Fig. 1. The cell presents a square shape and the electrodes are centred on the electrolyte. Most classically materials used for SOEC have been considered for the simulations: LSM for the anode, ZrO$_2$ stabilised with 8 mol% Y$_2$O$_3$ (8YSZ) for the electrolyte and Ni-8YSZ cermet for the cathode.

Interconnects are assumed to be made in ferritic stainless steel plates. A glass seal is positioned into a groove, which is machined in the metallic plate in order to prevent the gas leakage (Fig. 1).

Air and steam are introduced respectively at the anode and cathode sides by two gas manifolds designed into the interconnects and located at the electrodes gas inlet (Fig. 1). These manifolds ensure gas feeding into a pattern of triangular channels. As illustrated in Fig. 2, these channels distribute the gases on each electrode in a counter-flow configuration. The produced hydrogen and oxygen are finally exhausted from the SRU and collected by the two outlet gas manifolds, which are designed at the electrodes gas outlets (Fig. 1). The complete gas flow scheme (taken here for air) is represented in Fig. 3. Some typical dimensions of the SRU are listed in Table 1.

The coordinate system used for the modelling is shown in Figs. 1 and 3. A two dimensional approach has been adopted. The modelled surface is contained in the (x, y) plane (perpendicular to
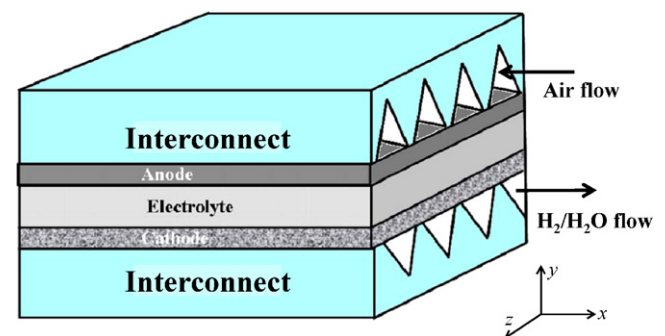

Fig. 2. Configurations for the oxygen and hydrogen flows along the electrodes (counter-flow configuration). The triangular shape of the anode and cathode gas channels is detailed.
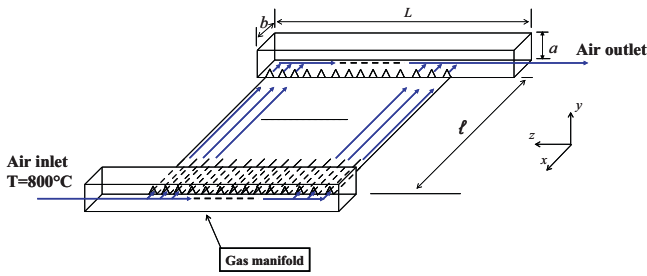
Fig. 3. Scheme of air flow in the SRU.

the z direction) and corresponds to an elementary slice taken in the middle of the SRU along a gas channel. Therefore, this approach neglects edge effects on the z direction.

The model has been divided into two connected modules: the electrochemical one and the thermal one. The electrochemical part of the model has been implemented in the software tool Matlab [19]. It allows determining the local current density, the distribution of gas species and the thermal sources related to the electrochemical reactions. The thermal module has been implemented in a finite element solver, Cast3M [20]. It allows determining the thermal fluxes and temperature field in both the solid and gas phases of the SRU. The two modules have been coupled through:

(i) the temperature field required to determine the kinetic constants of electro-chemical reactions,
(ii) the heat source terms necessary to simulate the temperature field,
(iii) the gas composition variation along the channels necessary to calculate the fluids thermal properties.

2.2. Description of the electrochemical module

2.2.1. Mass transfer

The pressure drop along the gas channels has been assumed to be negligible: atmospheric condition has been considered for the gas-phase pressure ($P_T = 1$ atm).

2.2.1.1. Gas flow along the anodic and cathodic channels. The variation of molar fractions along the gas channels (*i.e.* in the x direction) is caused by molar fluxes through the porous electrodes (*i.e.* in the y direction). This variation is calculated by using local mass balances performed for each species along the channels:

$$\frac{dn_i}{dx} = \gamma_i e N_i \tag{2}$$

where n_i denotes the molar flow rate in the channels for the specie i, N_i, the flux through the electrode, e, the width of the gas channel and, γ_i, a stoichiometric coefficient (equal to -1 for the reactant species and $+1$ for the product species).

2.2.1.2. Mass transport in the porous electrodes. In porous electrodes, the viscous flow, which is driven by a pressure gradient, is generally considered as negligible compared to the diffusive flow [21–23]. Therefore, the mass transport through the porous electrodes (*i.e.* in the y direction) has been described in the frame of

Table 1
Typical dimensions of the simulated SRU.

Electrodes length, ℓ (mm)	Manifold length, L (mm)	Manifold height, h (mm)	Manifold wide, b (mm)	Interconnect plate thickness, w (mm)
88	91	3	3	10

the DGM model, by combining the Stephan-Maxwell and Knudsen diffusion:

$$\frac{N_i}{D_{i,k}^{eff}} + \sum_{j=1, j \neq i}^{n} \frac{y_j N_i - y_i N_j}{D_{i,j}^{eff}} = -\frac{P_T}{RT}\left(\frac{dy_i}{dy}\right) \tag{3}$$

where y_i is the molar fraction of specie i and P_T the total pressure (=1 atm). The effective Knudsen and binary diffusion coefficients, $D_{i,k}^{eff}$ and $D_{i,j}^{eff}$, have been determined as a function of the electrodes microstructure parameters (*i.e.* mean pore radius $\bar{r}$, tortuosity factor τ and porosity ε). In porous media such as SOFC or SOEC electrodes, the following expressions are usually employed [24,25]:

$$D_{i,j}^{eff} = \frac{\varepsilon}{\tau} D_{i,j} \quad \text{and} \quad D_{i,k}^{eff} = \frac{\varepsilon}{\tau} D_{i,k} \tag{4}$$

The Knudsen diffusion coefficient can be assessed according to the kinetic theory of gases:

$$D_{i,k} = \bar{r}\frac{2}{3}\sqrt{\frac{8RT}{\pi M_i}} \tag{5}$$

where M_i denotes the molecular weight for the gas i. The binary diffusion coefficients have been expressed according to Todd and Young [26]:

$$D_{i,j} = \frac{0.00143 T^{1.75}}{P_T M_{i,j}^{1/2}(V_i^{1/3} + V_j^{1/3})^2} \quad \text{with} \quad M_{i,j} = 2/\left(\frac{1}{M_i} + \frac{1}{M_j}\right) \tag{6}$$

where V_i corresponds to the Füller diffusion volume.

At the anode side, the nitrogen flux is equal to 0 ($N_{N_2} = 0$) since this component is neither consumed nor produced. The oxygen release rate at the anode/electrolyte interface is given by the local current density i according to the Faraday's law (note that i is considered as its absolute value):

$$N_{O_2} = \frac{i}{4F} \quad \text{(for } y = \text{electrolyte thickness)} \tag{7}$$

Considering these conditions, the method used in [21] for integrating (3) in SOFC mode can be also applied for SOEC mode and leads to the expression of the oxygen molar fraction at the anode/electrolyte interface $y_{O_2}^{int}$:

$$y_{O_2}^{int} = 1 + (y_{O_2}^{canal} - 1)\exp\left(-\frac{RTi\delta_a}{4FD_{O_2}^{eff}P_T}\right) \quad \text{(for } P_T = 1\,\text{atm and } y$$

$$= \text{electrolyte thickness)} \tag{8}$$

where $y_{O_2}^{canal}$ is the oxygen concentration in the channel and δ_a the anode thickness.

At the cathode side, the nitrogen molar flux is also equal to 0 ($N_{N_2} = 0$). The fluxes related to the water consumption and hydrogen production at the cathode/electrolyte interface are also given by the Faraday's law:

$$N_{H_2O} = -N_{H_2} = \frac{i}{2F} \quad \text{(for } P_T = 1\,\text{atm and } y = 0) \tag{9}$$

A methodology detailed in Appendix A is proposed here to integrate the system of equations (3) in the case of a gas mixture composed of hydrogen, steam and nitrogen (used as a dilution gas). It allows determining the molar fractions at the cathode/electrolyte interface:

$$y_{N_2}^{int} = y_{N_2}^{canal} \times \exp\left(-k_1 \delta_c\right) \tag{10a}$$

$$y_{H_2}^{int} = y_{H_2}^{canal} + k_2\delta_c + \frac{k_3}{k_1} \times \left(y_{N_2}^{canal} - y_{N_2}^{canal}\exp\left(-k_1\delta_c\right)\right) \tag{10b}$$

$$y_{H_2O}^{int} = y_{H_2O}^{canal} + k_4\delta_c + \frac{k_5}{k_1} \times \left(y_{N_2}^{canal} - y_{N_2}^{canal}\exp\left(-k_1\delta_c\right)\right) \tag{10c}$$

Table 2
Microstructure and electrochemical parameters of cell layers.

Porosity, ε	Tortuosity factor, τ	Mean pore radius, $\bar{r}$ (μm)	
Microstructural parameters of both electrodes (anode and cathode)			
0.4	4	1	
Global contact resistances between electrodes/interconnects: $R_c = 0.1\ \Omega\ cm^2$ [27]			
Electrodes electronic conductivities: $\rho_{Ni\text{-}YSZ} = 800\ \Omega^{-1}\ cm^{-1}$ [33,34]; $\rho_{LSM} = 72\ \Omega^{-1}\ cm^{-1}$ [35]			

	Pre-exponential factors (mA cm^{-2})	Molar fraction exponent	Activation energy (KJ mol^{-1})
Exchange current densities			
Anode (LSM)	$B = 2.05 \times 10^8$	$p = 1/4$ [36,37]	120 [36]
Cathode (Ni-8YSZ)	$A = 1.26 \times 10^{10}$	$m = n = 1$ [36,38]	120 [36]

where $k_{i=1-5}$ are constants given in Appendix A, that depends on diffusion coefficients, local temperature and current density.

2.2.2. Cell voltage

Electrodes have been assumed to be good electrical conductors (Table 2) so that the electrical potential can be considered constant along the cell. Therefore, in the present model, the cell voltage is fixed and the local current density is calculated in order to verify the following equation along the cell length:

$$U_{cell} = E_{i=0} + \eta_{conc}^{anode} + \eta_{conc}^{cathode} + \eta_{act}^{anode} + \eta_{act}^{cathode} + R_{ohm}i \qquad (11)$$

with $E_{i=0}$ corresponds to the Open Circuit Voltage (OCV) expressed from the Nernst's equation:

$$E_{i=0} = E^0(T) + \frac{RT}{2F}\ln\frac{y_{H_2}^{TPB_c, i=0}\left(y_{O_2}^{TPB_a, i=0}\right)^{0.5}}{y_{H_2O}^{TPB_c, i=0}} \qquad (12)$$

where E^0 is the standard potential and y_j the partial pressures at OCV ($i = 0$) or under current ($i \neq 0$). The superscripts TPB_a and TPB_c denote the Triple Phase Boundaries at anode and cathode sides.

The terms η_{conc} and η_{act} in Eq. (11) are expressed considering their absolute values and correspond respectively to the concentration and activation overpotentials (at the anode or cathode side). The term $R_{ohm}i$ denotes the pure ohmic losses including (i) the ionic resistance of the electrolyte, R_e, (ii) electronic resistances of both electrodes, R_{LSM} and $R_{Ni\text{-}8YSZ}$, and (iii) the global contact resistances between the electrodes and the interconnects, R_c:

$$R_{ohm} = R_{LSM} + R_{Ni\text{-}8YSZ} + R_e + R_c \qquad (13a)$$

with ($S = 1\ cm^2$) $R_{LSM} = \dfrac{\delta_a}{\rho_{LSM}}$, $R_{Ni\text{-}8YSZ} = \dfrac{\delta_c}{\rho_{Ni\text{-}8YSZ}}$,

$$R_e = \frac{\delta_e}{\rho_{8YSZ}} \qquad (13b)$$

where ρ is the electrical conductivity of each considered material and δ the thickness of the anode, electrolyte or cathode layer. The contact resistance R_C is due to the current collection between electrodes and interconnects. The value of this parameter has been taken in the model to 0.1 Ω cm^2 [27] (Table 2). In planar configuration, electronic resistance of the electrodes is low compared to ohmic losses due to the electrolyte and can be regarded as temperature independent within the operating conditions [28]. Inversely, the ionic conductivity of the 8YSZ electrolyte has to be expressed as function of the operating temperature and is taken as [29]:

$$\rho_e\ (\Omega^{-1}\,cm^{-1}) = 466 \times \exp\left(\frac{-9934}{T\ (K)}\right) \qquad (14)$$

2.2.2.1. Activation overpotentials.

The activation overpotentials represent the voltage loss induced by the electrochemical reactions occurring at the electrodes/electrolyte interfaces. They can be expressed as a function of the current density from the Butler–Volmer equation:

$$i = i_{0,anode}\left\{\exp\left(\frac{2\alpha F\eta_{act}^{anode}}{RT}\right) - \exp\left(-\frac{2(1-\alpha)F\eta_{act}^{anode}}{RT}\right)\right\} \qquad (15a)$$

$$i = i_{0,cathode}\left\{\exp\left(\frac{2\alpha F\eta_{act}^{cathode}}{RT}\right) - \exp\left(-\frac{2(1-\alpha)F\eta_{act}^{cathode}}{RT}\right)\right\} \qquad (15b)$$

where $i_{0,anode}$ and $i_{0,cathode}$ represent respectively the anode and cathode exchange current densities. With the symmetrical factor α taken equal to 0.5, the activation overpotentials can be derived from Eqs. (15a) and (15b) [30,31]:

$$\eta_{act}^{anode} + \eta_{act}^{cathode} = \frac{RT}{F}\sinh^{-1}\left\{\frac{i}{2 \times i_{0,anode}}\right\}$$
$$+ \frac{RT}{F}\sinh^{-1}\left\{\frac{i}{2 \times i_{0,cathode}}\right\} \qquad (16)$$

The exchange current densities depend on (i) the temperature according to an Arrhenius law and (ii) to the reactant/product concentrations in the neighbourhood of the active sites (i.e. the TPBs) [32]:

$$i_0^{cathode} = A \times \left(y_{H_2}^{TPB_c}(i=0)\right)^m \times \left(y_{H_2O}^{TPB_c}(i=0)\right)^n \times e^{(-E_a^{cathode}/RT)} \qquad (17a)$$

$$i_0^{anode} = B \times \left(y_{O_2}^{TPB_a}(i=0)\right)^p \times e^{(-E_a^{anode}/RT)} \qquad (17b)$$

The values chosen for the activation energies E_a and the molar fraction exponents are reported in Table 2. These values have been determined on typical Ni-YSZ//YSZ//LSM cells operated in SOFC mode. The pre-exponential factors A and B have been scaled in order to obtain i_0 values recommended in literature [31,39]. It is have assumed in this work that these exchange current density expressions (17a) and (17b) were reasonably applicable to SOEC operation since temperature and reactant/product species are similar in both SOFC/SOEC operation modes.

2.2.2.2. Concentration overpotentials.

Potential losses can arise in operation because of the electrode inability to maintain the fluid initial composition in the gas-phase surrounding the TPBs. These concentration overpotentials are expressed from the Nernst's equation. They can be caused by insufficient diffusion through the electrodes or insufficient steam flow rate introduced at the SOEC inlet:

$$\eta_{conc}^{cathode} = \frac{RT}{2F}\ln\frac{y_{H_2O}^{TPB_c}(i=0) \times y_{H_2}^{TPB_c}(i\neq 0)}{y_{H_2O}^{TPB_c}(i\neq 0) \times y_{H_2}^{TPB_c}(i=0)} \qquad (18a)$$

$$\eta_{conc}^{anode} = \frac{RT}{4F}\ln\frac{y_{O_2}^{TPB_a}(i\neq 0)}{y_{O_2}^{TPB_a}(i=0)} \qquad (18b)$$

It can be noticed that the molar fraction at the TPB_a and TPB_c have been reduced in the present model at the anode/electrolyte and cathode/electrolyte interfaces respectively. It is worth noting that this assumption is well verified for sufficiently thick electrodes.
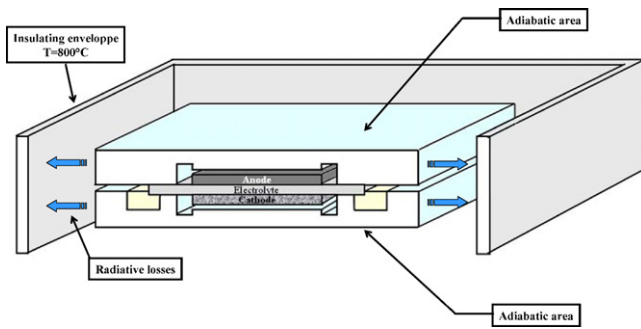
Fig. 4. Boundary conditions assumed for the thermal simulations.

Indeed, several studies [21,40,41] have shown that the reaction zone spreads on a limited region from the electrolyte/electrode into the electrode (~10 μm).

2.3. Description of the thermal module

2.3.1. Boundary conditions

Adiabatic conditions have been assumed for the surfaces connecting two adjacent SRUs (*i.e.* the bottom and top free surfaces of SRU as shown in Fig. 4). This assumption is rigorously right only for the SRUs located in the central region of the stack where heat flux in the stacking direction can be neglected.

The temperature of gases introduced into the SRU (*i.e.* at the two gas manifold inlets: see Fig. 3) have been taken equal to 800 °C. The temperature of the insulating envelope surrounding the stack is also supposed to be maintained at 800 °C. This last assumption corresponds to either a stack tested in a furnace, or a system in which the thermal fluxes exchanged with the SRU are managed.

2.3.2. Solid temperatures: energy balance for solid phases into the SRU

The governing equation to calculate the temperature field in the solids has been expressed considering conduction, convection and radiation. For a solid volume, dV, in contact with the fluid on a surface, dS, energy balance has been written as follows:

$$\lambda \left\{ div(grad(T)) \right\} dV + d\dot{Q} = h_{gas} dS \left\{ T_s - T_g \right\} + d\dot{\phi}_{rad}$$
$$\text{(conduction)} + \text{(heat sources)} = \text{(convection)} + \text{(radiation)} \quad (19)$$

The first term of this equation, $\lambda \left\{ div(grad(T)) \right\} dV$, is related to the heat transport by conduction in the solid phases. The term λ represents the thermal conductivity of the solid volume dV. It is worth noting that the porous anode and cathode have been modelled as homogenous media in which only conduction is taken into account. Indeed, the Peclet number Pe calculated within both electrodes remains much lower than unity, meaning that the heat transport by convection is negligible in comparison to conduction [42]. The effective thermal conductivity of the porous electrodes can then be determined considering a mixture law between the conductivities of solid and fluid regions [43].

2.3.3. Sources terms

The second term of Eq. (19), $d\dot{Q}$, corresponds to the heat sources related to the electrochemical reaction:

$$d\dot{Q} = \left\{ +\frac{i(x)}{2F} \Delta H_r - i(x)U_{cell} \right\} dS \quad (20)$$

where ΔH_r denotes the enthalpy of reaction for the steam dissociation into hydrogen and oxygen (see Eq. (1)). The heat sources include several contributions corresponding to the ohmic dissipations due to contact, electrodes, electrolyte resistances and heat

absorption due to the electrochemical reaction. Location within the SRU of these thermal sources is detailed in reference [18].

2.3.4. Gas temperatures for convective heat exchanges

Computation of the convective term in Eq. (19) requires the knowledge of the fluids temperatures T_g. These fluids temperatures must be determined all along the electrode lengths in the triangular-shaped channels (see Section 2.3.4.1) and (ii) into the manifolds at the inlet and outlet part of the electrodes (see Section 2.3.4.2).

2.3.4.1. Energy balance for fluids along the gas channels (in the x direction).
Because of the electrochemical reactions, the gas composition is modified along the triangular-channels between interconnect and electrodes. Therefore, the gas properties (*i.e.* heat capacity C_p, thermal conductivity λ, and dynamic viscosity η) depend on the position x along the channels. In this work, they have been calculated with the polynomial curves established by Todd and Young [26].

Gas inlet flow rates have been chosen in such way that a laminar flow takes place inside the channels (in the studied conditions, it has been found that the Reynolds number Re remains much lower than 1000 everywhere in the ducts of the simulated SRU). Furthermore, according to the results of Damn and Fedorov [44] and Sánchez et al. [45], the radiative heat exchange between gases and walls can be neglected. Finally, along the simulated triangular-shaped channels, the energy balances have been written as follows:

$$\sum_i \frac{\partial \left(n_i(x) C_p^i(x) T_g(x) \right)}{\partial x} dx = h_{steam}(x) dS \left\{ T_s(x) - T_g(x) \right\}$$

$$(i = H_2, H_2O, N_2) \quad (21a)$$

$$\sum_i \frac{\partial \left(n_i(x) C_p^i(x) T_g(x) \right)}{\partial x} dx = h_{air}(x) dS \left\{ T_s(x) - T_g(x) \right\}$$

$$(i = O_2, N_2) \quad (21b)$$

The term T_g denotes the temperature of fluids and T_s denotes the wall temperature of the solid phase. The exchange surface dS corresponds to the contact surface between gas and solid for the considered triangular-shaped channel. The heat transfer coefficients h_{steam} and h_{air} have been determined from the Nusselt number Nu:

$$h_{steam \text{ or } air}(x) = \frac{Nu \, \lambda_i(x)}{D_H} \quad i = O_2//N_2 \text{ or } i = H_2O//H_2//N_2 \quad (22)$$

where D_H is the hydraulic diameter of the cathode or anode channel. The determination of Nu number is potentially complex since it could be affected by many factors such as thermal gradient or heat flux heterogeneity. However, the thermal gradient remains limited in the present study (see Section 3.1.2). Furthermore, the Nusselt number tends to an asymptotic value, provided that a fully developed laminar flow is achieved in the channels. This condition is largely fulfilled in our configuration. As a consequence, the Nusselt number could be taken to $Nu = 3.68$ (*i.e.* the asymptotic value corresponding to a flow confined in channel) [46,47].

It is worth noting that fluids heat conductivities λ_i depend on the gas composition along the cell (Fig. 5). As a consequence, the heat transfer coefficient, which is linearly dependant of λ_i according to Eq. (22), will follow the same evolution. In electrolysis mode, steam is transformed into hydrogen all along the cathode. Since this gas component presents a much higher thermal conductivity than other species, the heat exchange coefficient $h_{steam}(x)$ can be
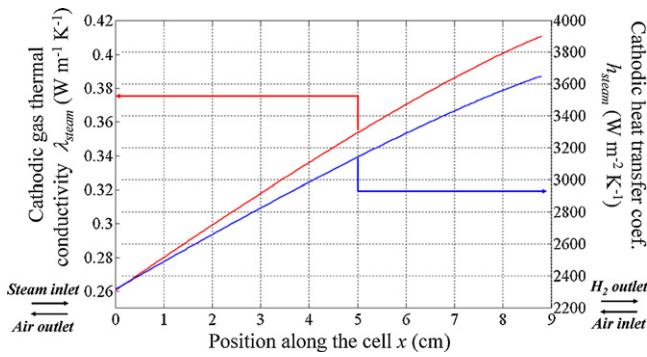
Fig. 5. Evolution of the fluid thermal conductivity and heat transfer coefficient plotted along the cathode channel. *Nu* number has been assumed constant along the channel (U_{cell} = 1.5 V, steam conversion rate = 96.2%, condition I of SRU gas feeding: see Table 4, active cell area = 77.44 cm^2).

strongly increased from the electrode inlet up to the outlet (Fig. 5). From this result, it appears that modification of the heat transfer coefficient along the cell has to be taken into account for SOEC modelling.

2.3.4.2. Fluids temperature into the manifolds. Convective heat exchanges have been taken into account for gas flowing into the manifolds:

- At the electrodes inlets, the calculation of steam (or air) temperature evolution in the z direction is provided in Appendix B. The convective heat fluxes introduced in Eq. (19) have been determined considering the gas temperature taken in the middle of the SRU (*i.e.* for $z = L/2$: see model assumptions in Section 2.1):

$$T_g = (T_{inlet} - T_s) \times \left\{ \frac{1}{2} \right\}^{(h2(a+b)L/n_{tot}C_p)}$$
$$+ T_s \quad \left(\text{for} \quad z = \frac{L}{2} \quad \text{and} \quad T_{inlet} = 800\,^\circ\text{C} \right) \quad (23)$$

where T_g is the steam (or air) temperature into the manifold. T_{inlet} and n_{tot} are respectively the fluid temperature and molar flow rate introduced in the SRU.

- At the electrodes outlet, the gas temperature into the manifold has been assumed to be the same that the one taken at the outlet of the triangular-shaped channels (*i.e.* for $x = \ell$ and $z = L/2$).

2.3.5. Radiative heat exchanges

The last term of Eq. (19), $d\dot{\varphi}_{rad}$, is related to the heat transfer by radiation and has been divided into two contributions:

- The first one, $d\dot{\varphi}_1$, corresponds to the solid surface-to-surface heat exchange between electrodes (anode or cathode) and interconnects plates. It has been approximated in the model according to the general expression between two infinite parallel planes:

$$d\dot{\varphi}_1 = \left\{ \frac{\sigma \varepsilon_{anode/cathode} \varepsilon_{interconnect}}{1 - \left(1 - \varepsilon_{anode/cathode}\right)\left(1 - \varepsilon_{interconnect}\right)} \left(T_{anode/cathode}^4 - T_{interconnect}^4\right) \right\} dS \tag{24}$$

where ε denotes the emissivity of materials (for anode, cathode and interconnects) and σ the Stefan–Boltzmann's constant.

- The second contribution to $d\dot{\varphi}_{rad}$ corresponds to the radiative heat losses, $d\dot{\varphi}_2$, flowing from the SRU to the stack insulating envelope:

$$d\dot{\varphi}_2 = \left\{ \sigma \varepsilon_{interconnect} \left(T_s^4 - T_{insulating}^4\right) \right\} dS \tag{25}$$

where T_s denotes the surface temperature taken on the free edge of the SRU. The term $T_{insulating}$ corresponds to the stack envelope temperature taken here at 800 °C (Fig. 4). The thermal parameters for materials considered in the model are provided in Table 3.

The model reliability can be considered as good since it is based on usual physics for the studied SOEC application. Furthermore, the model derived from a SOFC one [17,18] which has been already validated. It can be noticed that experimental validation of the present model is on going and will be published later.

3. Simulation results and analysis

3.1. Simulations of a case taken as reference: mechanisms involved in the steam electrolysis

3.1.1. Simulation conditions for the case taken as reference

A reference case has been defined in order to analyse the mechanisms involved in the steam electrolysis. In this reference case, an Electrolyte Supported Cell (ESC) with anode, electrolyte and cathode thicknesses respectively fixed to 50, 90 and 50 μm is integrated in the SRU. The cell active area is taken to 77.44 cm^2.

Simulations have been carried out for the first condition of gas feedings detailed in Table 4. These conditions have been chosen to achieve a high steam conversion (SC) rate at U_{cell} = 1.5 V in such way that the mass and energy transports phenomena associated to the overpotentials are exacerbated. It can be noticed that the same steam and hydrogen molar flow rate is supplied at the cathode side: R defined as the ratio of n_{H_2} over n_{H_2O}, $R = n_{H_2}/n_{H_2O}$, is equal to the unity. Moreover, the dilution of hydrogen and steam into nitrogen is limited: ξ expressed as $\xi = n_{N_2}/(n_{H_2} + n_{H_2O} + n_{N_2})$ is taken to 0.1.

Air ratio λ is defined as the air molar flow rate introduced at the anode inlet divided by the cathode molar flow rate ($\lambda = n_{air}/n_{cath.gas}$).

Table 3
Thermal parameters.

	Cathode	Electrolyte	Anode	Interconnect	Glass seal
Conductivity, λ (W m^{-1} K^{-1})	6 [43]	3.8 [48]	11 [43]	25 [49]	1.0[a]
Emissivity, ε	0.4 [43]	–	0.4 [43]	0.7 [50]	–

[a] Estimated with correlations provided in ref. [51] considering a commercial glass seal (Schott 8422).

Table 4
Simulated molar flow rates (active cell area = 77.44 cm^2).

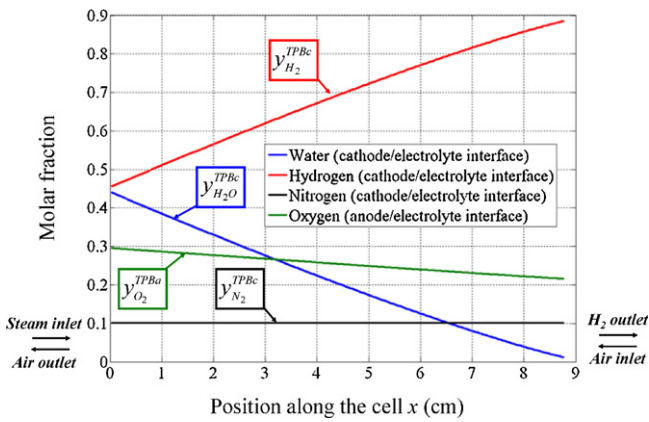| Gas feeding condition	Cathode gas mixture of H$_2$O, H$_2$ and N$_2$			Anode gas (air)	
	n_{H_2O} ($\times 10^{-6}$ mol s^{-1} cm^{-2})	$R = n_{H_2}/n_{H_2O}$	$\xi = n_{N_2}/(n_{H_2} + n_{H_2O} + n_{N_2})$	n_{air} ($\times 10^{-6}$ mol s^{-1} cm^{-2})	$\lambda = n_{air}/n_{cathodic\ gas}$
I (reference)	6.9034	1/1	1/10	30.682	2
II	6.9034	1/9	1/2	30.682	2
III	6.9034	1/1	1/2	55.227	2

Fig. 6. Evolution of the molar fraction along the cell length in the reference case (U_{cell} = 1.5 V, steam conversion rate = 96.3%, condition I of cell gas feeding, $\delta_{electrolyte}$ = 90 μm, δ_{anode} = $\delta_{cathode}$ = 50 μm, cell active area = 77.44 cm^2).

This parameter is taken to 2 in order to obtain a sufficient air flow rate, and hence, to maintain a substantial convective heat transfer at the anode side.

3.1.2. Evolution of molar fractions, overpotentials and temperature along the cell length

The variations of the output parameters of the model along the cell length are presented for a steam conversion rate SC = 96.3% corresponding to a cell voltage equal to 1500 mV. Fig. 6 illustrates the evolution of molar fractions calculated here at the electrochemical interfaces. The steam concentration is found to be decreased from the cathode inlet up to the cathode outlet, since this specie is consumed by the electrochemical reaction (1a). Accordingly, hydrogen is continuously produced and its molar fraction is raised from the cathode inlet up to the outlet. At the anode side, the oxygen is produced by reaction (1b), and hence, its molar fraction increases from the anode inlet up to the anode outlet.

Fig. 7 shows the evolution of the local current density along the cell length. The current slightly decreases from the anode inlet up to the outlet. This trend is consistent with the steep increase of the cathode concentration overpotential η_{conc}^{cath} calculated along the cell length and shown in Fig. 8. This pronounced increase can be attributed to the major water depletion associated to the high steam conversion rate (SC = 96.3%).

It is worth noting that the H_2O or H_2 molar fraction gradients along the y-axis between the gas channel and the cathode/electrolyte interface remains negligible all along the cell
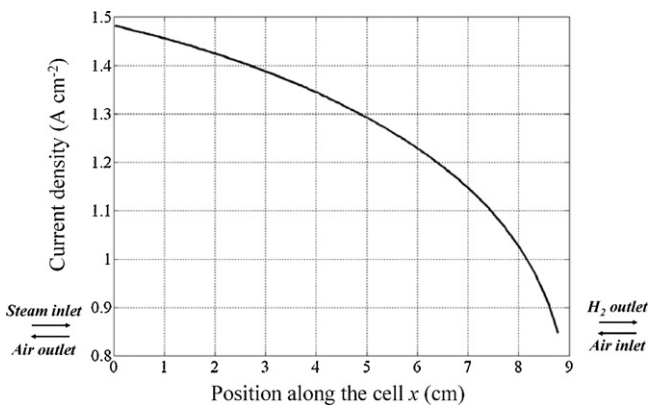
length ($\Delta y_{H_2 \text{ or } H_2O} < 0.01$). This result means that the gas transfer, either steam or hydrogen, through the thin cathode is not a limiting step for the electrochemical reaction.

As shown in Fig. 8, the ohmic voltage losses $R_{ohm} \times i$ and the anode activation overpotentials η_{act}^{anode} are found to follow the same evolution than the current density along the cell length and represent the highest contributions to cell voltage losses. Inversely, the anode concentration overpotential is found to be very low. This can be attributed to the air ratio that is sufficiently high to avoid a strong O_2 enrichment of the anodic gas.

Fig. 9 gives the temperature profiles along the cell length calculated at the cathode/electrolyte interface and in the interconnect plate. In the SRU, temperatures are found to vary between 852 and 865 °C. This temperature range is consistent with the exothermal operation mode chosen in this reference case (U_{cell} = 1.5 V). It can be noticed that the temperature profiles are approximately symmetrical along the channel length. This temperature evolution is due to the heat accumulated into the cathode and anode gases flowing in opposite direction (i.e. in a counter-flow configuration). Moreover, the heat fluxes removed from the solid structure are mainly exhausted by radiation symmetrically on each side on the SRU. It can also be noticed that the temperature maximum is slightly shifted from the middle of the cell towards the steam inlet. This phenomenon is consistent with the extent of the electrochemical reaction along the cell length: the reaction is favoured at the steam inlet where the current density is the highest (cf. Fig. 7).
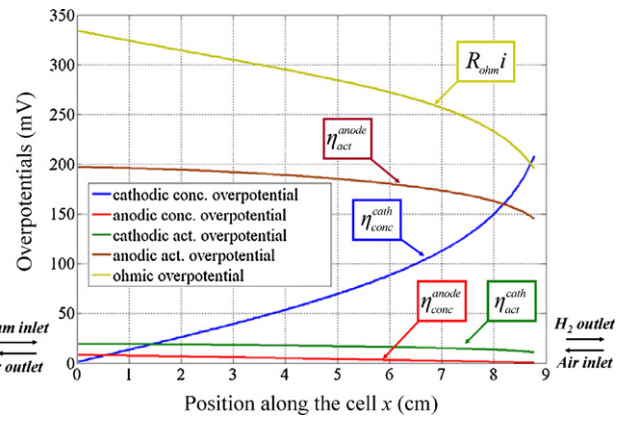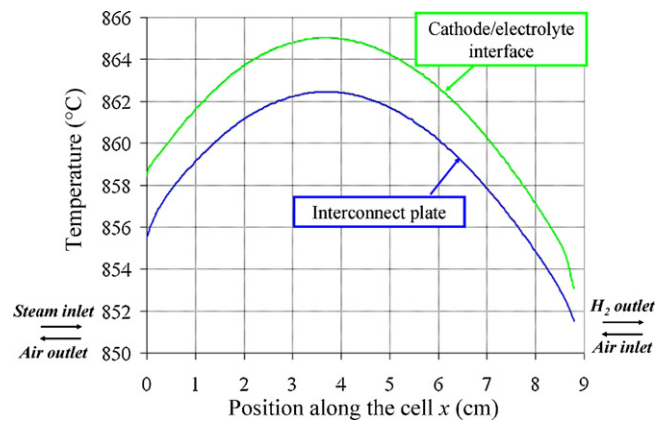

Fig. 8. Evolution of the overpotential along the cell length in the reference case (U_{cell} = 1.5 V, steam conversion rate = 96.3%, condition I cell gas feeding, $\delta_{electrolyte}$ = 90 μm, δ_{anode} = $\delta_{cathode}$ = 50 μm, cell active area = 77.44 cm^2).

Fig. 7. Evolution of the local current density along the cell length in the reference case (U_{cell} = 1.5 V, steam conversion rate = 96.3%, condition I cell gas feeding, $\delta_{electrolyte}$ = 90 μm, δ_{anode} = $\delta_{cathode}$ = 50 μm, cell active area = 77.44 cm^2).

Fig. 9. Temperature evolution plotted as a function of the cell length in the reference case (U_{cell} = 1.5 V, steam conversion rate = 96.3%, condition I cell gas feeding, temperature of the interconnect plate taken on the surface connecting two adjacent SRUs, $\delta_{electrolyte}$ = 90 μm, δ_{anode} = $\delta_{cathode}$ = 50 μm, cell active area = 77.44 cm^2).

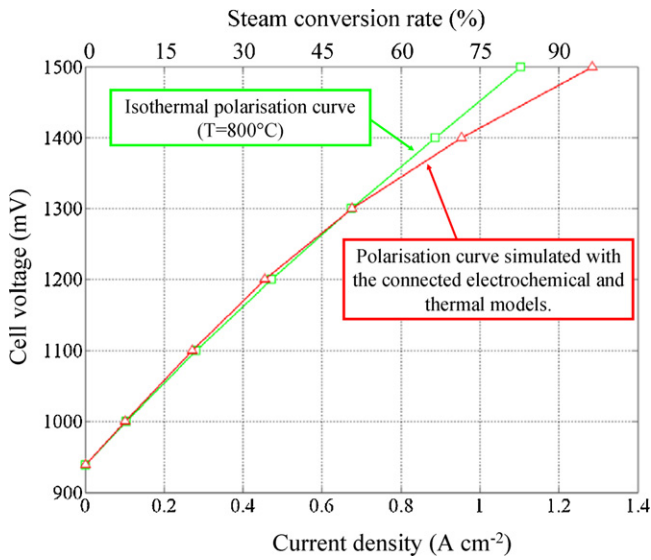**Fig. 10.** Polarisation curves obtained: (i) simulated in the isothermal state ($T = 800\,°C$) and (ii) simulated with the connected electrochemical and thermal model taking into account thermal variations with operation modes (reference case, condition I cell gas feeding, $\delta_{electrolyte} = 90\,\mu m$, $\delta_{anode} = \delta_{cathode} = 50\,\mu m$, cell active area = 77.44 cm^2).

The temperature of the interconnect plate is found to be close to the cell temperature (Fig. 9). This low thermal gradient in the stacking direction (y direction) is due to the adiabatic assumption considered here for the modelling.

3.1.3. Effect of cell polarisation

Fig. 10 provides two polarisation curves simulated in the reference case. These curves have been computed either:

(i) by considering a "virtual" isothermal operating state at $T = 800\,°C$ (*i.e.* by neglecting any thermal effect),
(ii) or by coupling the thermal and electrochemical models. The thermal variations are then associated with endothermic and exothermic operation modes. In this case, the variation of cell temperature with the current density (or cell voltage) is given in Fig. 11.
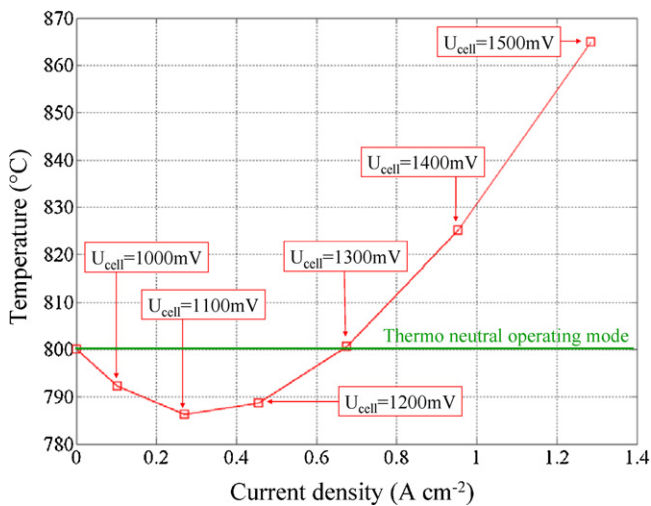

Fig. 11. Cell temperature plotted as a function of the current density and thermal sources (reference case, condition I cell gas feeding, the temperature has been taken in the middle of the cell at the cathode/electrolyte interface, $\delta_{electrolyte} = 90\,\mu m$, $\delta_{anode} = \delta_{cathode} = 50\,\mu m$, cell active area = 77.44 cm^2).

When the cell operates at the thermo neutral voltage ($\sim$1.28 V), heat sources released in the cell such as ohmic losses are counterbalanced by the endothermic nature of the electrolysis reaction. As a consequence, the cell temperature is found to be equal to 800 °C (Fig. 11). In this operating condition, the current density is found to be the same as the one computed in the "virtual" isothermal state ($\sim$0.68 A cm^{-2} at $U_{cell} = 1.28$ V) (Fig. 10).

Below the thermo neutral voltage, heat sources do not counterbalance the endothermic electrolysis reaction and the cell temperature is found to be lower than 800 °C (Fig. 11). As a consequence, the cell performance calculated in this case is lower than the one obtained in the isothermal assumption. However, the differences between the two curves remain extremely slight.

Inversely, above the thermo neutral voltage, the cell warming and its impact on the cell polarisation curve are more pronounced. However, it has been calculated that the activation and concentration overpotentials are not significantly impacted by the cell warming. As a consequence, the cell performance improvement observed above the thermo neutral voltage cannot be explained by the activation or concentration overpotentials decrease. Actually, this phenomenon must be attributed to the decrease of the electrolyte ionic resistance with the temperature increase. This effect is illustrated in Fig. 12: above the thermo neutral voltage, the ohmic losses calculated in the "virtual" isothermal state are much higher than the ones simulated by coupling the thermal and electrochemical models. It can be seen in Fig. 12 that the difference in the ohmic losses between the two cases is $\Delta(R_{ohm}i) \approx 40$ mV at 1.0 A cm^{-2}. This value corresponds roughly to the cell polarisation curve improvement calculated at the same current density in Fig. 10.

3.2. Sensitivity analysis: effect of geometrical and operation parameters on steam electrolysis

3.2.1. Impact of hydrogen over steam ratio introduced at the cathode side

The effect of cathodic gas composition has been investigated considering the Electrolyte Supported Cell configuration ($\delta_{anode} = \delta_{cathode} = 50\,\mu m$ and $\delta_{electrolyte} = 90\,\mu m$). The SRU performances have been simulated with the first and second conditions of gas feedings, for which the H$_2$ over H$_2$O ratio R is decreased from 1/1 to 1/9 (see Table 4).

The steam molar flow rate is kept constant for both simulated cases. That condition allows obtaining identical SC rates according to the applied current densities. This remark means that the overpotentials induced by the steam depletion along the cell are identical in both simulations. It can be also mentioned that the total
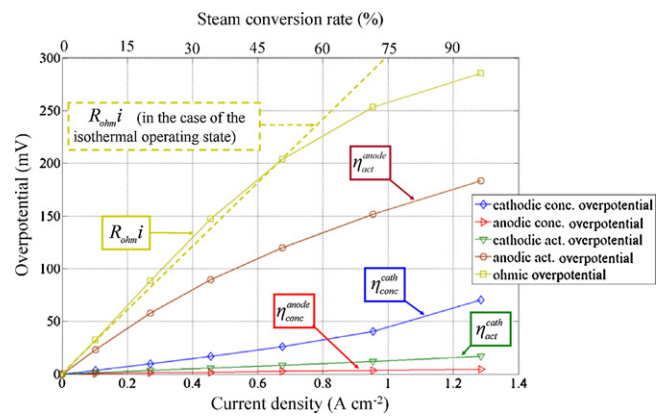

Fig. 12. Overpotential plotted as a function of current density and SC rate calculated: (i) in the isothermal state for the dashed line and (ii) by coupling the thermal and electrochemical models for the solid curves (reference case, condition I cell gas feeding, $\delta_{electrolyte} = 90\,\mu m$, $\delta_{anode} = \delta_{cathode} = 50\,\mu m$, cell active area = 77.44 cm^2).

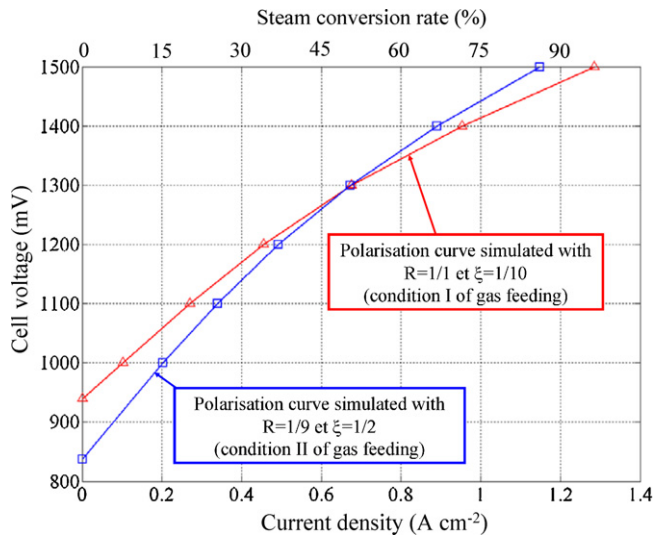**Fig. 13.** Polarisation curves simulated for conditions I and II of gas feedings ($\delta_{electrolyte} = 90\,\mu m$, $\delta_{anode} = \delta_{cathode} = 50\,\mu m$, cell active area = 77.44 cm²).

molar flow rate and air ratio are maintained to the same levels in such way that the thermal conditions (in terms of heat convective flow) are similar in both simulated cases. The balance when decreasing H_2 molar flow rate is achieved by increasing N_2 molar flow rate (*i.e.* by increasing the dilution term ξ).

A significant difference has been found between the two simulated polarisation curves (Fig. 13). As it is expected by considering Eq. (12), the OCV at $R = 1/1$ is found to be higher than the one calculated at $R = 1/9$. Whatever the investigated current density, it can be seen that the Area Specific Resistance (ASR) is lower for $R = 1/1$ than for $R = 1/9$. The contributions to the voltage losses have to be analysed to understand this result:

- As expected, the SRU temperature fields have been found to be close to each other. As a consequence, the voltage losses due to the ohmic resistances are quite similar in both simulated cases.
- Since the condition of air supply is the same for both polarisation curves, the anodic activation and concentration overpotentials are found to be not impacted by the modification of the cathode gas composition.
- Finally, the difference between the two polarisation curves is found to be mainly induced by the increase of cathode activation overpotential, η_{act}^{cath} (Fig. 14a), and in a lower extent, by the increase of cathode concentration overpotential η_{conc}^{cath} (Fig. 14b). The impact of the cathode gas composition onto η_{act}^{cath} is ascribed to the dependence of the exchange current density i_0 with hydrogen and steam molar fraction (see Eq. (17a)). Therefore, it can be inferred from this result that the activation overpotentials can be increased from negligible values to substantial ones according to the condition of cathodic gas supply.

3.2.2. Impact of geometric cell configuration

Electrolyser performances have been assessed considering a stack assembled with Cathode Supported Cells (CSC) fabricated with the same materials as taken previously in the ESC case. The simulations have been carried out for a thickness of the cermet substrate equal to 1000 μm. Thin electrolyte and anode layers deposited onto the cathode support have been fixed respectively to 15 μm and 50 μm. The polarisations curves have been computed with the first and third conditions of gas feedings (see Table 4). These simulated curves are compared in Fig. 15 to the one calculated in the reference case (*i.e.* for the Electrolyte Supported Cell and for the first condition of gas feeding).

At the thermo neutral voltage and considering the same operating conditions, the CSC geometry exhibits better performances than the ESC configuration. This behaviour is obviously induced by the difference in the ionic resistances between the two kinds of cells. However, at the highest investigated cell voltages, it can be seen that the gap in performances between CSC and ESC tends to vanish. Indeed, the cell temperature elevation decreases the YSZ ionic resistivity and its relative contribution to the overall cell overpotentials. Moreover, the thick cathode substrate of the CSC geometry hinders the diffusion trough the electrode. The resulting mass transfer limitation induces large concentration overpotentials and leads to the limiting current density observed on the polarisation curve (Fig. 15). For instance, at $i = 1.2\,A\,cm^{-2}$ and SC = 90%, the term η_{conc}^{cath} is increased from ~61 mV for ESC to ~228 mV for CSC (considering the first condition of gas feeding). In this last case, the drop of H_2 or H_2O molar fraction across the thick cathode becomes significant as shown in Fig. 16.

3.2.3. Impact of gas dilution through the cathode

Considered the CSC geometry, the high concentration overpotentials have been correlated to a mass transfer limitation. This
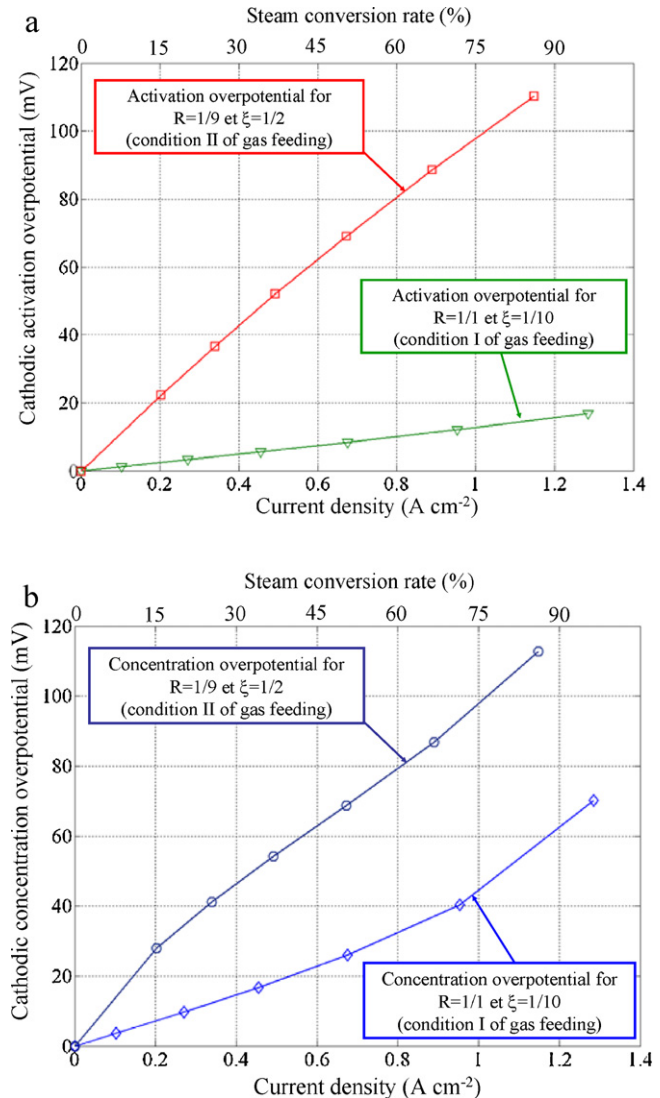

Fig. 14. Cathode overpotentials computed with conditions I and II of gas feedings ($\delta_{electrolyte} = 90\,\mu m$, $\delta_{anode} = \delta_{cathode} = 50\,\mu m$, cell active area = 77.44 cm²): (a) activation overpotential η_{act}^{cath}. (b) concentration overpotential η_{conc}^{cath}.
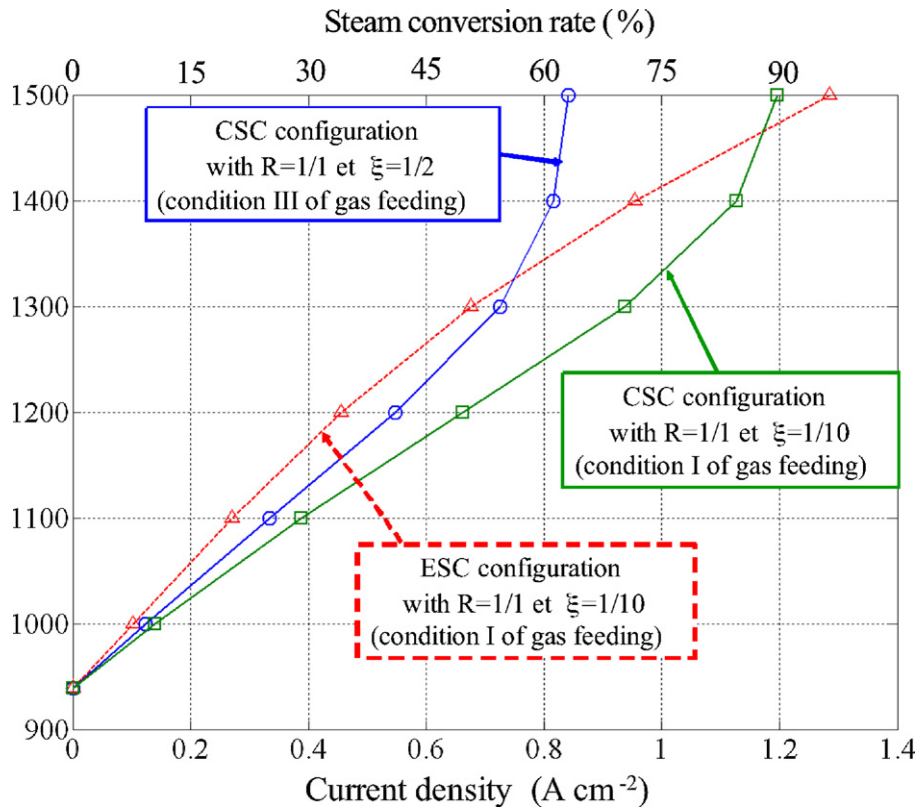
Fig. 15. Polarisation curves simulated for conditions I or III of gas feedings: solid line: CSC ($\delta_{cathode}$ = 1000 μm, $\delta_{electrolyte}$ = 15 μm, δ_{anode} = 50 μm, cell active area = 77.44 cm^2). Dashed line: ESC ($\delta_{electrolyte}$ = 90 μm, δ_{anode} = $\delta_{cathode}$ = 50 μm, cell active area = 77.44 cm^2).

effect is found to be worsened when the steam and hydrogen mixture is diluted into a neutral gas. For instance, the limiting current density is roughly decreased from ~1.2 A cm^{-2} to ~0.84 A cm^{-2}, when the dilution rate ξ is raised from the first to the third condition of gas feeding (Fig. 15). As a consequence, addition of diluents into H$_2$, H$_2$O mixture leads to a decrease in the cell performances.

This effect of diluent concentration on cell limiting current is consistent with the results obtained in SOFC mode by Jiang and Virkar [22]. These authors have shown that the maximum achievable current density by the fuel cell is limited at high concentrations of diluent. This phenomenon is explained by the hydrogen and steam effective gas diffusivity which is lowered with increasing the nitrogen concentration. Indeed, it can be easily demonstrated with

Fig. 16. Evolution of the H$_2$ and H$_2$O molar fraction along the CSC cell length (U_{cell} = 1.5 V, steam conversion rate = 90%, condition I of cell gas feeding, $\delta_{cathode}$ = 1000 μm, $\delta_{electrolyte}$ = 15 μm, δ_{anode} = 50 μm, cell active area = 77.44 cm^2).

Eqs. (A1-2) and (A1-3) that the H$_2$ and H$_2$O effective diffusivities depend on the N$_2$ concentration as followed:

$$D_{H_2}^{eff} = \left\{ \frac{1}{D_{H_2,k}^{eff}} + \frac{y_{N_2}}{D_{H_2,N_2}^{eff}} + \frac{1-y_{N_2}}{D_{H_2,H_2O}^{eff}} \right\}^{-1} \quad \text{with}$$

$$N_{H_2} = -\frac{P_T}{RT} D_{H_2}^{eff} \frac{dy_{H_2}}{dy} \quad \text{(Fick's law)} \tag{26}$$

$$D_{H_2O}^{eff} = \left\{ \frac{1}{D_{H_2O,k}^{eff}} + \frac{y_{N_2}}{D_{H_2O,N_2}^{eff}} + \frac{1-y_{N_2}}{D_{H_2,H_2O}^{eff}} \right\}^{-1} \quad \text{with}$$

$$N_{H_2O} = -\frac{P_T}{RT} D_{H_2O}^{eff} \frac{dy_{H_2O}}{dy} \quad \text{(Fick's law)} \tag{27}$$

It can be noticed that the H$_2$O/N$_2$ binary effective diffusion coefficient is lower than the one for H$_2$O/H$_2$ species (D_{H_2O,N_2}^{eff} = 2.858 × 10^{-5} m^2 s^{-1} < D_{H_2O,H_2}^{eff} = 1.004 × 10^{-4} m^2 s^{-1}). In this case, according to Eq. (27), the term $D_{H_2O}^{eff}$ is decreased with increasing the concentration of diluent y_{N_2}. This trend is illustrated in Fig. 17 where the steam effective diffusion coefficient has been plotted as function of nitrogen molar fraction.

4. Discussion

4.1. Effect of radiative heat losses on the stack temperature

As shown in Fig. 11, the SRU maximum temperature reaches roughly 865 °C at 1500 mV and for $i \sim 1.28$ A cm^{-2}. In this case, it is worth underlining that the main part of heat sources is removed by the radiation losses. Indeed, 73% of the heat generated by the electrochemical process within the cell is dissipated by radiative
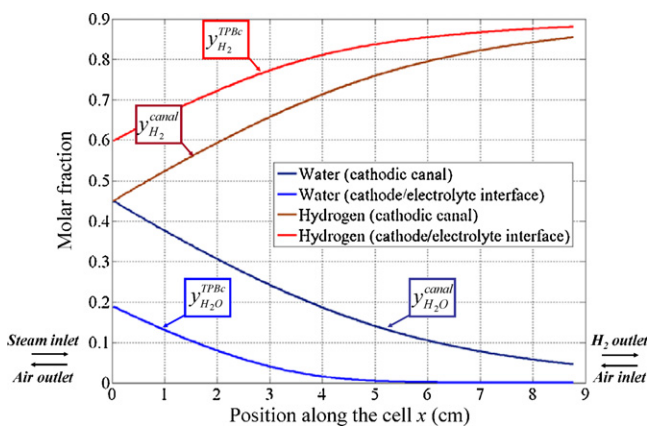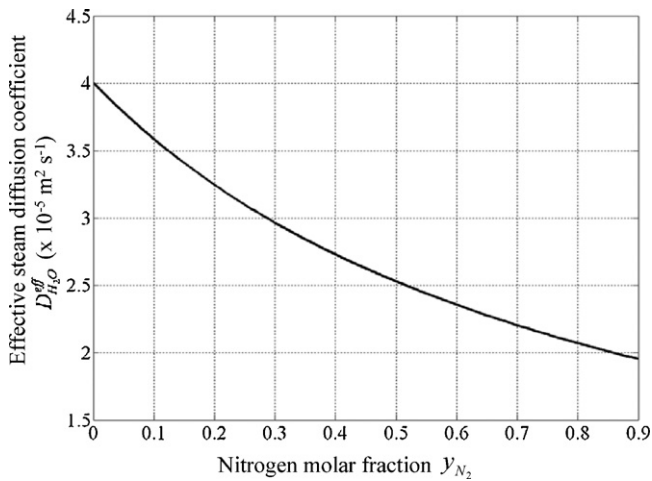
Fig. 17. Effective steam diffusion coefficient $D_{H_2O}^{eff}$ plotted as a function of N_2 molar fraction ($T = 800\,°C$, $\varepsilon = 0.4$, $\bar{r} = 1\,\mu m$, $P_T = 1\,atm$).

transfer between the SRU and the insulating envelope. Only 27% of the remaining heat sources are transferred to anode and cathode gas streams. It can be inferred from this result that the radiative losses have a determinant impact on the cell temperature: the radiation between the stack and its insulating envelope appears to be the most efficient thermal transfer mode to evacuate (or bring) the heat generated (or absorbed) by the electrolysis process. Conversely, the convective heat transfer remains limited along the gas channels. As a consequence, the radiation represents the main heat transfer mode and it cannot be neglected in the steam electrolysis modelling.

Because of its significant importance, the stack temperature should strongly depend on the radiation efficiency. To assess this effect, a sensitivity analysis has been carried out by varying the factor A which links the radiative losses to the solid temperatures: $A = \int_{\dot{\varphi}} d\dot{\varphi}_2 / \left(T_s^4 - T_{insulating}^4 \right)$ (see Eq. (25)). In Fig. 18, the simulated cell temperature is plotted as a function of this factor A. The percentages of radiative and convective heat losses have been also added into the figure. It can be seen that the relative proportions of heat removed by radiation and convection remain in the same order of magnitude whatever the value of A (since the thermal sources are equal for each simulated points). When the "efficiency" of the radi-
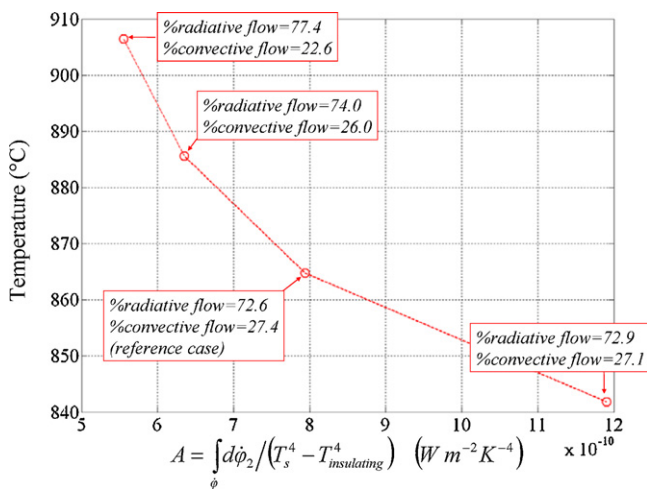

Fig. 18. Cell temperature plotted as a function of A ($U_{cell} = 1.5\,V$, Condition I cell gas feeding, the temperature has been taken in the middle of the cell at the cathode/electrolyte interface, $\delta_{electrolyte} = 90\,\mu m$, $\delta_{anode} = \delta_{cathode} = 50\,\mu m$, cell active area = 77.44 cm²).

ation is lowered by decreasing A, the cell temperature is observed to be strongly increased. Indeed, the solid temperature has to be raised to maintain a sufficient radiative heat flow and, hence, to evacuate the heat generated within the cell. This phenomenon maintains the energy balance between the heat sources and the radiation and convection fluxes. As a consequence, a limitation of the radiation heat exchange into the electrolyser stack will lead to an increase of the SRU temperature. This temperature elevation could be detrimental regarding to the metal interconnect plates or the contact layers. Moreover, the SRU ageing processes will be accelerated at this temperature level. In this case, an operating condition close to the thermo neutral voltage will be the only way to keep a reasonable temperature within the SRU solid structure.

4.2. Effect of activation and concentration overpotentials on the electrolyser performances

4.2.1. Activation overpotential

As mentioned in Section 3.1, a substantial contribution to the cell polarisation has been attributed to the anode activation overpotential η_{act}^{anode} (Figs. 8 and 12), while the cathode activation polarisation η_{act}^{cath} represents only a small part of the cell voltage losses. Although the term η_{act}^{cath} can be significantly affected by the H_2/H_2O ratio as shown in Section 3.1 (Fig. 14), the global electrochemical behaviour of the electrolyser cannot be strongly deteriorated by this overpotential (Fig. 13). That means that H_2/H_2O ratio can be chosen according to other criteria such as cell materials, durability or system efficiency.

4.2.2. Concentration overpotential

In the present simulated conditions, the anodic concentration overpotential η_{conc}^{anode} contributes less than 20 mV to the irreversible losses (Fig. 12). This result means that this contribution remains insignificant whatever the investigated operating conditions and cell configurations.

For the ESC, the cathodic concentration overpotential η_{conc}^{cath} reaches only moderate values even at high current densities and SC rate. For instance, this overpotential represents approximately ~11% of the total voltage losses at $i = 1.2\,A\,cm^{-2}$ and SC = 90% (in the reference case).

Conversely, considering the CSC design, the cathodic concentration overpotential η_{conc}^{cath} is liable to provide a large contribution to the cell polarisation. For instance, this overpotential represents up to ~41% of the irreversible losses at $i = 1.2\,A\,cm^{-2}$ and SC = 90% (condition I of gas feeding and $h_{cathode} = 1000\,\mu m$). Furthermore, the η_{conc}^{cath} polarisations are exacerbated when diluents are added into the steam and hydrogen mixture (see Section 3.2.3). These high cathode concentration overpotentials have been ascribed to a mass transfer limitation through the thick cathode. Because of this limitation, the difference between the CSC and ECS designs tends to vanish at high current density and SC rate (although the CSC configuration exhibits better performances than ESC geometry at intermediate cell polarisation: Fig. 15). It is worth underlining that this effect will depend strongly on the thickness of the cathode substrate. As it is illustrated in Fig. 19, the cell limiting current is increased and its associated cathode concentration overpotentials are decreased when the thickness of the support is reduced. For instance, when the cathode thickness is decreased to 600 μm, the term η_{conc}^{cath} is lowered below 50 mV at 0.8 A cm⁻² (Fig. 19b). It can be noticed that this last value is consistent with the simulation result established by Udagawa et al. [13] in similar conditions.

As a consequence, the thinning of the cermet substrate improves the cell performances but also reduced its mechanical robustness. Therefore, a compromise remains to be found from this point of view. Improvements of gas transport in the porous cathode could help to obtain these requirements.
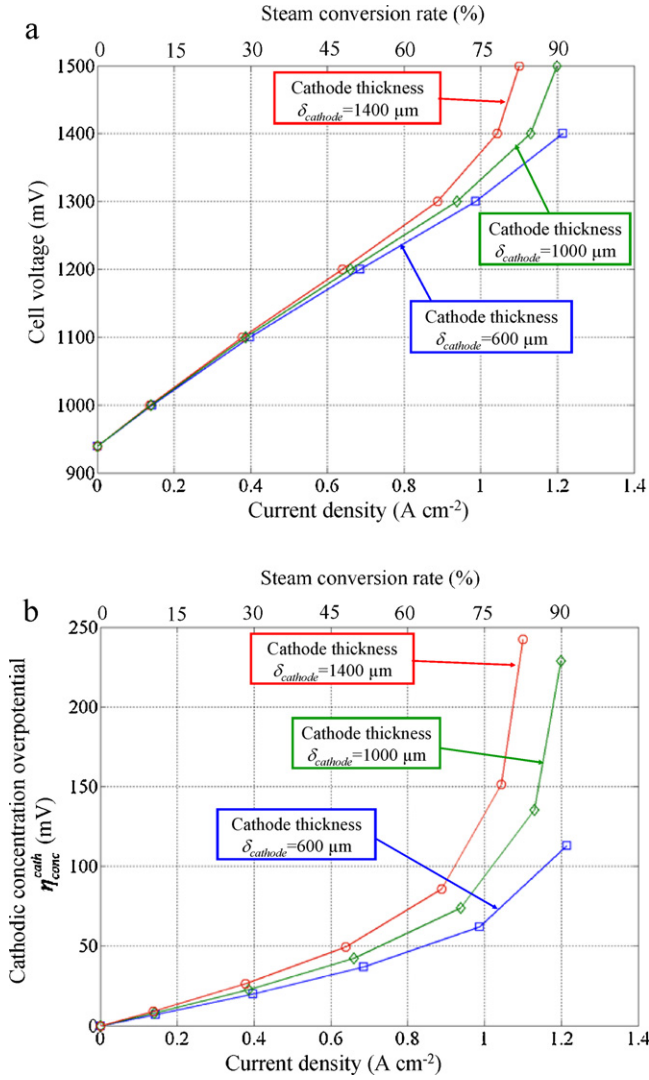
Fig. 19. Effect of cathode thickness on CSC electrochemical behaviour (condition I of gas feeding, $\delta_{electrolyte} = 15\,\mu\text{m}$, $\delta_{anode} = 50\,\mu\text{m}$, cell active area = 77.44 cm^2). (a) Polarisation curves. (b) Cathodic concentration overpotential plotted as a function of current density.

In addition, it has been found that the contribution to the gas transport of both molecular and Knudsen diffusions is roughly in the same order of magnitude. Then, if one of these diffusion processes is neglected in the modelling, the simulation results will underestimate the cathode concentration overpotential.

5. Conclusion

A 2D multi-physic in-house-model has been developed to analyse the performances of SOEC stack. The model encompasses a combined electrochemical and thermal description of the electrolyser. In order to facilitate the numerical implementation, an analytical solution for multi-species diffusion across the porous cathode was derived from the DGM equations.

Understandable predictions of SOEC behaviour can be achieved by using the model since it provides all the important parameters of the stack operation: distribution of local temperature, heat fluxes, current densities, gas concentrations and overpotentials.

Simulations have shown that thermal equilibrium of the stack is strongly dependant on radiative heat losses with the insulating envelope. In the exothermic operation mode, the cell temperature depends on the radiation efficiency: in order to avoid a too high

temperature increase of the SRU, an operating condition close to the thermo neutral voltage is necessary.

Parametric study has been carried out to analyse the SOEC irreversible losses. It has been found that anode activation overpotentials are significant. Conversely, the polarisation due to the cathode activation is much more restricted. Thus, even if this activation overpotential depends on the steam and hydrogen molar fraction introduced at the cathode inlet, the H_2/H_2O ratio can be fixed according to other criteria such as cell materials, durability or system efficiency.

The anode concentration overpotentials have been found to be insignificant whatever the operating condition. The cathode concentration overpotentials are found to be moderate for ESC design, while they can increase drastically with current density for CSC geometry. Finally, addition of diluent into the H_2, H_2O mixture increases these overpotentials since the effective gas diffusion of steam is substantially lowered.

Acknowledgments

Appendix A. Steam, hydrogen and nitrogen diffusion through the porous cathode

The DGM model (see Eq. (3)) is applied for a gas mixture composed of hydrogen, steam and nitrogen. It leads the three following expressions:

$$\left(-\frac{P_T}{RT}\right)\frac{dy_{N_2}}{dy} + \left(\frac{N_{H_2O}}{D^{eff}_{N_2,H_2O}} + \frac{N_{H_2}}{D^{eff}_{N_2,H_2}}\right)y_{N_2}$$
$$-\left(\frac{1}{D^{eff}_{N_2,k}} + \frac{y_{H_2O}}{D^{eff}_{N_2,H_2O}} + \frac{y_{H_2}}{D^{eff}_{N_2,H_2}}\right)N_{N_2} = 0 \tag{A1-1}$$

$$\left(-\frac{P_T}{RT}\right)\frac{dy_{H_2}}{dy} + \left(\frac{N_{H_2O}}{D^{eff}_{H_2,H_2O}} + \frac{N_{N_2}}{D^{eff}_{H_2,N_2}}\right)y_{H_2}$$
$$-\left(\frac{1}{D^{eff}_{H_2,k}} + \frac{y_{H_2O}}{D^{eff}_{H_2,H_2O}} + \frac{y_{N_2}}{D^{eff}_{H_2,N_2}}\right)N_{H_2} = 0 \tag{A1-2}$$

$$\left(-\frac{P_T}{RT}\right)\frac{dy_{H_2O}}{dy} + \left(\frac{N_{H_2}}{D^{eff}_{H_2O,H_2}} + \frac{N_{N_2}}{D^{eff}_{H_2O,N_2}}\right)y_{H_2O}$$
$$-\left(\frac{1}{D^{eff}_{H_2O,k}} + \frac{y_{H_2}}{D^{eff}_{H_2O,H_2}} + \frac{y_{N_2}}{D^{eff}_{H_2O,N_2}}\right)N_{H_2O} = 0 \tag{A1-3}$$

Eqs. (A1-1)–(A1-3) constitute a set of 3 equations including 3 unknowns (i.e. y_{N_2}, y_{H_2} and y_{H_2O}). Since neither consumption nor production of nitrogen occurs at the cathode side (meaning that $N_{N_2} = 0$), Eq. (A1-1), can be written as followed:

$$\frac{dy_{N_2}}{dy} = k_1 \times y_{N_2} \tag{A1-4}$$

with

$$k_1 = \frac{R \times T}{P_T} \left(\frac{N_{H_2}}{D^{eff}_{N_2,H_2}} + \frac{N_{H_2O}}{D^{eff}_{N_2,H_2O}} \right)$$

This last differential equation can be solved considering the boundary condition, $y_{N_2} = y^{canal}_{N_2}$ when $y = \delta_c$:

$$y_{N_2} = y^{canal}_{N_2} \times \exp\left\{ k_1 \left(y - \delta_c\right) \right\} \tag{A1-5}$$

The expression of the molar fraction of nitrogen at the cathode/electrolyte interface is directly deduced from (A1-5):

$$y^{int}_{N_2} = y^{canal}_{N_2} \times \exp\left(-k_1 \delta_c\right) \tag{A1-6}$$

Assuming that no accumulation of species occurs in operation (i.e. $N_{H_2} + N_{H_2O} = 0$) and with $y_{H_2} + y_{H_2O} + y_{N_2} = 1$, Eq. (A1-2) can be written:

$$k_2 + k_3 \times y_{N_2} = -\frac{dy_{H_2}}{dy} \tag{A1-7}$$

with

$$k_2 = \frac{R \times T}{P_T} \left(\frac{N_{H_2}}{D^{eff}_{H_2,k}} + \frac{N_{H_2}}{D^{eff}_{H_2,H_2O}} \right)$$

$$k_3 = \frac{R \times T}{P_T} \left(\frac{N_{H_2}}{D^{eff}_{H_2,N_2}} - \frac{N_{H_2}}{D^{eff}_{H_2,H_2O}} \right)$$

The boundary condition of Eq. (A1-7) corresponds to $y_{H_2} = y^{canal}_{H_2}$ when $y = \delta_c$. The solution of this differential equation corresponds to:

$$y_{H_2} = y^{canal}_{H_2} + k_2 \delta_c + \frac{k_3}{k_1} y^{canal}_{N_2} - k_2 y - \frac{k_3}{k_1} y^{canal}_{N_2} \exp\left\{ k_1(y - \delta_c) \right\} \tag{A1-8}$$

At the cathode/electrolyte interface, this expression becomes:

$$y^{int}_{H_2} = y^{canal}_{H_2} + k_2 \delta_c + y^{canal}_{N_2} \frac{k_3}{k_1} \left\{ 1 - \exp(-k_1 \delta_c) \right\} \tag{A1-9}$$

Considering the same previous assumptions, Eq. (A1-3) can be also written:

$$k_4 + k_5 \times y_{N_2} = -\frac{dy_{H_2O}}{dy} \tag{A1-10}$$

with

$$k_4 = \frac{R \times T}{P_T} \left(\frac{N_{H_2O}}{D^{eff}_{H_2O,k}} + \frac{N_{H_2O}}{D^{eff}_{H_2O,H_2}} \right)$$

$$k_5 = \frac{R \times T}{P_T} \left(\frac{N_{H_2O}}{D^{eff}_{H_2O,N_2}} - \frac{N_{H_2O}}{D^{eff}_{H_2,H_2O}} \right)$$

Integration of this last differential equation allows determining the steam molar fraction at the cathode/electrolyte interface:

$$y^{int}_{H_2O} = y^{canal}_{H_2O} + k_4 \delta_c + y^{canal}_{N_2} \frac{k_5}{k_1} \left\{ 1 - \exp(-k_1 \delta_c) \right\} \tag{A1-11}$$

It is worth noting that the constants k_1, k_2, k_3, k_4 and k_5 can be expressed as function of the current density by using Eq. (9). Therefore, Eqs (A1-6), (A1-9) and (A1-11) can be used to calculate the gas composition at the cathode/electrolyte interface as a function of the molar fractions in the channel and the local current density.

Appendix B. Temperature of fluid into the gas manifold

The aim of this section is to determine the gas temperature evolution along the manifold at the anode or cathode inlets (Fig. 1). These gas temperature evolutions $T_g(z)$ are determined by writing an energy balance between z and $z + dz$:

$$n(z)C_p \left\{ T_g(z + dz) - T_g(z) \right\} = 2(a + b) dz \times h \times \left\{ T_s - T_g(z) \right\} \tag{A2-1}$$

where C_p and $n(z)$ are respectively the specific heat and the molar flow rate of the gas mixture. The terms a and b denote respectively the manifold width and height. As illustrated in Fig. 3, the molar flow rate $n(z)$ depends on the z coordinate along the canal:

$$n(z) = n_{tot} \times \left\{ 1 - \frac{z}{L} \right\} \tag{A2-2}$$

where n_{tot} is the total molar flow rate introduced into the SRU and L the manifold length.

Eqs. (A2-1) and (A2-2) lead to the following first-order differential equation:

$$n_{tot} \left\{ 1 - \frac{z}{L} \right\} C_p \times \frac{dT_g(z)}{dz} + h2(a + b) \times T_g(z) = h2(a + b) T_s \tag{A2-3}$$

This last equation can be solved assuming that the wall temperature of the solid phase T_s is constant in the z direction (cf. model assumption in Section 2.1):

$$T_g(z) - T_s \propto \left\{ n_{tot} \left\{ 1 - \frac{z}{L} \right\} \right\}^{((h2(a+b)L)/n_{tot}C_p)} \tag{A2-4}$$

At the SRU inlet, $T_g(z = 0) = T_{inlet} = 800\,^\circ C$:

$$T_g(z) = (T_{inlet} - T_s) \times \{n_{tot}\}^{((-h2(a+b)L)/n_{tot}C_p)}$$
$$\times \left\{ n_{tot} \left\{ 1 - \frac{z}{L} \right\} \right\}^{((h2(a+b)L)/n_{tot}C_p)} + T_s \tag{A2-5}$$

References

[1] C.C. Elam, C.E. Gregoire Padró, G. Sandrock, A. Luzzi, P. Lindblad, E. Fjermestad Hagen, Int. J. Hydrogen Energy 28 (2003) 601–607.
[2] M. Zahid, J. Schefold, A. Brisse, Hydrogen and Fuel Cells, Fundamentals, Technologies and Applications, Wiley-VCH, Weinheim, Germany, 2010, pp. 227–242.
[3] D.L. Stojic, M.P. Marceta, S.P. Sovilj, S.S. Miljanic, J. Power Sources 118 (2003) 315–319.
[4] M. Ni, K.H. Michael, Leung, Y.C. Dennis, Leung, Int. J. Hydrogen Energy 33 (2008) 2337–2354.
[5] L Mingyi, Y. Bo, X. Jingming, C. Jing, J. Power Sources 177 (2008) 493–499.
[6] W. Dönitz, R. Schmidberger, Int. J. Hydrogen Energy 7 (1982) 321–330.
[7] S.H. Jensen, P.H. Larsen, M. Mogensen, Int. J. Hydrogen Energy 32 (2007) 3253–3257.
[8] A. Brisse, J. Schefold, M. Zahid, Int. J. Hydrogen 33 (2008) 5375–5382.
[9] J.R. Mawdsley, J.D. Carter, A.J. Kropf, B. Yildiz, V.A. Maroni, Int. J. Hydrogen Energy 34 (2009) 4198–4207.
[10] C.M. Stoots, J.E. O'Brien, K.G. Condie, L. Moore-McAteer, J.J. Hartvigsen, D. Larsen, INL report, INL/EXT-09-17023, 2009. http://www.inl.gov/technicalpublications/Documents/4408284.pdf.
[11] M. Ni, M.K.H. Leung, D.Y.C. Leung, Int. J. Hydrogen Energy 32 (2007) 2305–2313.
[12] M. Ni, M.K.H. Leung, D.Y.C. Leung, Electrochem. Acta 52 (2007) 6707–6718.
[13] J. Udagawa, P. Aguiar, N.P. Brandon, J. Power Sources 166 (2007) 127–136.
[14] J. Udagawa, P. Aguiar, N.P. Brandon, J. Power Sources 180 (2008) 46–55.
[15] J.S. Herring, J.E. O'Brien, C.M. Stoots, G.L. Hawkes, J.J. Hartvigsen, M. Shahnam, Int. J. Hydrogen Energy 32 (2007) 440–450.
[16] D. Grondin, J. Deseure, A. Brisse, M. Zahid, P. Ozil, J. Appl. Electrochem. 40 (2010) 933–941.
[17] B. Morel, J. Laurencin, Y. Bultel, F. Lefebvre-Joud, J. Electrochem. Soc. 152 (7) (2005) A1382–A1389.
[18] J. Laurencin, F. Lefebvre-Joud, G. Delette, J. Power Sources 177 (2008) 355–368.
[19] http://www.mathworks.fr/products/matlab/.
[20] http://www-cast3m.cea.fr/cast3m/index.jsp.
[21] J.W. Kim, A.V. Virkar, K.Z. Fung, K. Metha, S.C. Singhal, J. Electrochem. Soc. 146 (1) (1999) 69–78.
[22] Y. Jiang, A.V. Virkar, J. Electrochem. Soc. 150 (7) (2003) A942–A951.
[23] T. Ackmann, L.G.J. de Haart, W. Lehnert, D. Stolten, J. Electrochem. Soc 150 (6) (2003) A783–A789.
[24] Y. Shi, N. Cai, C. Li, J. Power Sources 164 (2007) 639–648.

[25] L. Andreassi, G. Rubeo, S. Ubertini, P. Lunghi, R. Bove, Int. J. Hydrogen Energy 32 (2007) 4559–4574.
[26] B. Todd, J.B. Young, J. Power Sources 110 (2002) 186–200.
[27] J.W. Fergus, Mater. Sci. Eng. A 397 (2005) 271–283.
[28] C. Stiller, B. Thorud, S. Seljebø, Ø. Mathisen, H. Karoliessen, O. Bolland, J. Power Sources 146 (2005) 227–240.
[29] A. Weber, E. Ivers-Tiffée, J. Power Sources 127 (2004) 273–283.
[30] S.H. Chan, K.A. Khor, Z.T. Xia, J. Power Sources 93 (2001) 130–140.
[31] S.H. Chan, Z.T. Xia, J. Appl. Electrochem. 32 (2002) 339–347.
[32] C. Déportes, M. Duclot, P. Fabry, J. Fouletier, A. Hammou, M. Kleitz, E. Siebert, J.L. Souquet, Electrochimie des solides, Ed. Presses Universitaires de Grenoble, 1994.
[33] D. Simwonis, F. Tietz, D. Stöver, Solid State Ionics 132 (2000) 246–251.
[34] S.T. Aruna, M. Muthuraman, K.C. Patil, Solids State Ionics 111 (1998) 45–51.
[35] Mizusaki, N. Mori, H. Takai, Y. Yonemura, H. Minamiue, H. Tagawa, M. Dokiya, H. Inaba, K. Naraya, T. Sasamoto, T. Hashimoto, Solids State Ionics 132 (2000) 167–180.
[36] P. Costamagna, K. Honegger, J. Electrochem. Soc. 145 (11) (1998) 3995–4007.
[37] E. Achenbach, J. Power Sources 49 (1994) 333–348.
[38] M. Mogensen, T. Lindergaard, in: S.C. Singal, T. Iwahara (Eds.), Proceedings of SOFC III (Electrochem. Soc.), Pennington, PV 93-4, 1993, p. 484.
[39] P.-W. Li, M.K. Chyu, J. Power Sources 124 (2003) 487–498.
[40] S.B. Adler, Solids State Ionics 111 (1998) 125–134.
[41] S. Primdahl, M. Mogensen, J. Electrochem. Soc. 144 (10) (1997) 3409–3418.
[42] T. Ackmann, L.G.J. de Haart, W. Lehnert, D. Stolten, J. Electrochem. Soc. 150 (6) (2003) A783–A789.
[43] J.M. Klein, Y. Bultel, S. Georges, M. Pons, Chem. Eng. Sci. 62 (2007) 1636–1649.
[44] D.L. Damn, A. Fedorov, J. Power Sources 143 (2005) 158–165.
[45] D. Sánchez, R. Chacarteguei, A. Muñoz, T. Sánchez, J. Power Sources 160 (2006) 1074–1087.
[46] Y.-P. Chyou, T.-D. Chung, J.-S. Chen, R.-F. Shie, J. Power Sources 139 (2005) 126–140.
[47] W.M. Rohsenhow, J. Hartnett, E. Ganic, Handbook of Heat Transfer Fundamentals, second ed., McGraw-Hill, New York, 1973.
[48] A.H. Heuer, L.W. Hobbs (Eds.), Science and Technology of Zirconia, vol. 5, The Am. Ceramic Society, p. 655.
[49] D. Larrain, J. Van Herle, F. Maréchal, D. Favrat, J. Power Sources 131 (2004) 304–312.
[50] http://www.engineeringtoolbox.com/emissivity-coefficients-d_447.html.
[51] M.K. Choudhary, R.M. Potter, in: D.L. Pye, A. Montenaro, I. Joseph (Eds.), Chap. 9 in "Properties of Glass-formation Melts, CRC Press, May 2005.